

Correcting the Relative Bias of Light Obscuration and Flow Imaging Particle Counters

Dean C. Ripple¹ · Zhishang Hu²

Received: 24 February 2015 / Accepted: 26 October 2015 / Published online: 10 November 2015
© Springer Science+Business Media New York (outside the USA) 2015

ABSTRACT

Purpose Industry and regulatory bodies desire more accurate methods for counting and characterizing particles. Measurements of proteinaceous-particle concentrations by light obscuration and flow imaging can differ by factors of ten or more.

Methods We propose methods to correct the diameters reported by light obscuration and flow imaging instruments. For light obscuration, diameters were rescaled based on characterization of the refractive index of typical particles and a light scattering model for the extinction efficiency factor. The light obscuration models are applicable for either homogeneous materials (e.g., silicone oil) or for chemically homogeneous, but spatially non-uniform aggregates (e.g., protein aggregates). For flow imaging, the method relied on calibration of the instrument with silica beads suspended in water-glycerol mixtures.

Results These methods were applied to a silicone-oil droplet suspension and four particle suspensions containing particles produced from heat stressed and agitated human serum albumin, agitated polyclonal immunoglobulin, and abraded ethylene tetrafluoroethylene polymer. All suspensions were measured by two flow imaging and one light obscuration apparatus. Prior to correction, results from the three instruments

disagreed by a factor ranging from 3.1 to 48 in particle concentration over the size range from 2 to 20 μm . Bias corrections reduced the disagreement from an average factor of 14 down to an average factor of 1.5.

Conclusions The methods presented show promise in reducing the relative bias between light obscuration and flow imaging.

KEY WORDS flow imaging · flow microscopy · light obscuration · particle · protein aggregate

NOTATION

$a_1 \dots a_4$	Parameters in Eq. 10
A_p	Projected area of a particle
b	Feret diameter
b_{max}	Maximum Feret diameter of a particle consistent with constructive interference of light scattering
c	Measured diameter minus actual diameter of silica beads
C_d	Correction factor for refractive index related to particle diameter, Eq. 3
C_{sca}	Scattering cross section
$C_{w/t}$	Correction factor for refractive index related to particle width-to-thickness ratio, Eq. 3
d	Diameter
d_{act}	Actual diameter
d_c	Cut-off diameter, above which Q is obtained by a scaling relation
d_{meas}	Measured diameter
d_{trans}	Transformed diameter
F	Fraction of pixels with largest absolute magnitude of φ
G	Parameter to assess validity of RGD theory, $G=2k/(m-1)$
k	Wavenumber, equal to $2\pi/l$

This paper is a contribution of the United States government and is not subject to copyright

Electronic supplementary material The online version of this article (doi:10.1007/s11095-015-1817-9) contains supplementary material, which is available to authorized users.

✉ Dean C. Ripple
dean.ripple@nist.gov

¹ Biomolecular Measurement Division, National Institute of Standards and Technology, Gaithersburg, Maryland, USA

² Center for Computational and Systems Biology, Institute of Biophysics, Chinese Academy of Sciences, Beijing, China

l	Largest characteristic length of a particle
m	Reduced refractive index, equal to the ratio of the refractive index to the refractive index of the matrix liquid
n_p	Average refractive index of a particle immersed in a matrix liquid
n_l	refractive index of the matrix liquid
$N(d)$	Cumulative particle size distribution, equal to the number of particles per unit volume of equivalent diameter d or larger
Q	Extinction efficiency factor
Q_{PSL}	Extinction efficiency factor for polystyrene latex beads
Q'	Modified extinction efficiency factor equal to the total scattering beyond the aperture angle, divided by the average projected area of a randomly oriented spheroid.
r_{ij}	Distance between spheres i and j
R_N	Ratio of the maximum and minimum values of $N(d)$
x, y	Orthogonal distances perpendicular to the optical axis
t	Particle thickness of a gravitationally settled particle
w	Particle width, equal to the minimum Feret diameter, of a gravitationally settled particle
z	Distance along the optical axis
z_p	Thickness of a particle in the z direction
α	Minimum angle for light to be scattered out of a light-obscuration detector
Δn	Refractive index of a particle minus the refractive index of the matrix fluid
η	Aspect ratio of minor to major axis.
θ	Scattering angle
λ_0	Wavelength in vacuum
λ	Wavelength in the matrix fluid
φ	Optical phase thickness

ABBREVIATIONS

ETFE	Ethylene tetrafluoroethylene
FI	Flow imaging
HEPES	2-[4-(2-hydroxyethyl)piperazin-1-yl]ethanesulfonic acid
HSA	Human serum albumin
IgG	Immunoglobulin G
LO	Light obscuration
PFA	Perfluorinated alkoxy
PMMA	Poly(methyl methacrylate)
PSL	Polystyrene latex
PVDF	Polyvinylidene fluoride
QPI	Quantitative phase imaging
RGD	Rayleigh-Gans-Debye
SDS	Sodium dodecyl sulfate

INTRODUCTION

Because particles formed by the aggregation of proteins are potentially immunogenic (1–5), methods are needed to size and count these protein particles accurately. Pharmacopeial methods for detection of particles at diameters below 100 μm include filter microscopy and light obscuration (LO) (6,7). Protein particles are difficult to observe by filter microscopy, but light obscuration is in routine use for the characterization of particle levels in protein-based biotherapeutics. In the past few years, flow imaging (FI) has become popular for particle characterization (8,9). The method has the capability to provide greater morphological information, to distinguish between different particle types (10,11), and to have less sensitivity to the low optical contrast of typical protein particles (12).

The literature provides multiple examples of FI producing particle counts a factor of 2 to 10, and occasionally higher, than counts obtained by LO (12–17). The diameter reported by an LO particle counter is the diameter of a polystyrene latex (PSL) bead that has the same total optical cross-section as the particle being measured. The primary cause of this difference has been attributed to the low refractive index difference between the protein particles and the matrix fluid, which leads to reduced light scattering and undersizing of the particles, relative to the PSL beads used for instrument calibration (15,18,19). The irregular morphology of protein particles may also affect the instrument response.

Flow imaging particle counters measure the projected area of particles passing through a flow cell. The projected area can be converted to an equivalent circular diameter equal to the diameter of a circle of the same area as the measured particle. Due to the limited optical resolution of FI systems, the measured projected area may be in error due to optical diffraction effects or due to the particle being out of focus.

The primary focus of this paper is to transform the diameter reported by both FI and LO instruments into a diameter that is closer to the actual equivalent circular diameter of the average particle cross section. We demonstrate that adjustment of the diameter values alone suffices to greatly reduce the relative bias of FI and LO instruments. For the FI instruments, a simple five-point calibration using silica beads suffices to reduce the relative bias between the two FI instruments used in this work. This approach is adequate for the relatively low level of monomer protein and excipients in the studied samples, but at high protein or excipient concentration the response of the FI instruments varies with particle refractive index. In the future, we hope to identify practical methods for correcting the bias of FI instruments when the particle refractive index varies with particle diameter and is spatially inhomogeneous.

For correction of the LO diameters, we present a theoretical model for the light scattering from these particles and show how such a model may be used to correct the bias

between light obscuration and flow imaging methods. The simple LO model does account for variation in particle refractive index and inhomogeneity.

To assess the success of the method, we have measured both silicone-oil droplets and four types of particles with low optical contrast by LO and FI. The measured particle samples included: agitated solutions of human serum albumin (HSA) and polyclonal immunoglobulin (IgG), heat-stressed HSA solutions, and abraded ethylene tetrafluoroethylene (ETFE). The ETFE particles are a proposed reference material that mimics the optical, morphological and size properties of protein particles. The droplet and particle suspensions were measured using two different FI instruments and one LO instrument to obtain $\mathcal{N}(d)$, the particle concentration for particles of equivalent diameter of d and greater. A convenient measure of the agreement of multiple data sets is the ratio R_N of the maximum and minimum values of $\mathcal{N}(d)$ from the set of three instruments, at fixed d . Prior to correction, this ratio for the four types of particle suspensions ranged from 3.1 to 48 over the size range from 2 to 20 μm , with an average ratio of 14.5. After correction of instrument biases, the disagreement in the region of overlap (5 to 25 μm) reduced to an average R_N value in the range from 1.3 to 1.7. The reduction in relative bias (from 14.5 to ≈ 1.5) is highly encouraging, but success does require knowledge of the refractive index of the particles. The Discussion section addresses this limitation. But in many circumstances, the insight gained by the model can be useful in interpreting LO data.

Application of the bias corrections described in this paper requires a number of non-standard theoretical and experimental techniques which are covered in detail in the Methods section. As a result the Methods section is particularly extensive and technically detailed. The Results and Discussion sections present the results of these corrections in a more approachable manner. The Conclusions discuss the possible uses of our results.

MATERIALS AND METHODS

Materials

Silica beads of reported 1.57 and 6.1 μm diameter were obtained from Bangs Laboratories (Fishers, IN).¹ Silica beads of nominal diameter of 2.88, 10.3 and 25.0 μm were obtained from Corpuscular Inc. (Cold Spring, NY).

Polymethylmethacrylate (PMMA) beads of a nominal size range (63 to 75) μm were obtained in dry form from

Cospheric (Santa Barbara, CA), and at sizes of 5, 10 and 20 μm in aqueous suspensions from Phosphorex (Hopkinton, MA). We formed suspensions in water by adding beads to either water, a water/glycerol mixture, or a mineral oil of known refractive index (National Institute of Standards and Technology (NIST) Standard Reference Material (SRM®) 1922), shaking vigorously for 40 s, and then sonicating for 60 s. When adding the beads to mineral oil, either dry beads were used or a drop of the aqueous suspension was first dried at 70°C. Glass beads used were from NIST SRM® 1003C and 1021.

Glycerol (ACS Reagent Grade, from Mallinckrodt Baker, Phillipsburg, NJ) was diluted with ultrafiltered water to the desired concentration (Barnstead NANOpure system, Dubuque, IA) and then filtered through a 0.22 μm , polyvinylidene fluoride (PVDF) membrane filter (Millipore GV syringe filter) prior to use. Lack of appreciable particles in the water and water-glycerol solutions was confirmed by measurement by light obscuration and flow microscopy. 2-pyridine methanol was obtained from Sigma Aldrich and filtered through PVDF filters prior to use. The refractive index of prepared mixtures was measured at the sodium D line (589 nm wavelength), using an Abbe refractometer that had been calibrated using ultrafiltered water and NIST SRM 1922. Silicone oil (12,500 centistokes nominal viscosity, Brookfield Engineering, Middleboro, MA) and polysorbate 20 (Genetex, Irvine, CA) were used as received for preparing suspensions of silicone droplets.

Experimental Methods

Preparation of Silicone Oil Suspensions

Suspensions of silicone oil droplets were prepared following the recipe of Vandesteeg and Kilbert (20). Briefly, silicone oil at a mass fraction of 0.1% was added to a buffer consisting of 10 mmol/L phosphate buffer (pH 7.4), 150 mmol/L NaCl, and 0.02% mass concentration polysorbate 20. The mixture was sonicated for 15 min, diluted 500:1 with additional buffer and then aliquoted into three precleaned polycarbonate bottles.

Preparation of Particle Suspensions

Suspensions of protein particles were prepared by both heating (HSA only) and agitating (HSA and polyclonal IgG) buffered protein solutions.

For the heat-induced protein particles, HSA protein solution at a concentration of 1 mg/mL was prepared in a 50 mL centrifuge tube by dilution of nominal 30% mass concentration HSA (Sigma Aldrich, St. Louis, MO, USA) into sodium phosphate buffer (pH 7.0, 0.03 mol/L sodium phosphate, 0.03 mol/L sodium chloride). UV-vis absorption

¹ Certain commercial equipment, instruments, or materials are identified in this document. Such identification is not intended to imply recommendation or endorsement by the National Institute of Standards and Technology, nor is it intended to imply that the products identified are necessarily the best available for the purpose.

measurements at 280 nm were used to determine the dilution factor of 1 part HSA solution to 374 parts of buffer. Prior to use, centrifuge tubes and 22 mL, perfluorinated alkoxy (PFA) screw-top vials had been precleaned by agitation in ultrafiltered water (Barnstead NANO pure system, Dubuque, IA) for 4 times. The diluted HSA protein solution was filtered through a 0.22 μm , PVDF membrane filter (Millipore GV syringe filter) into a precleaned PFA screw-top vial. In addition to the protein solution, 1 blank of filtered phosphate buffer solution was also prepared in a PFA vial. Both HSA protein solution and the phosphate buffer blank were put into an oven and exposed to 70°C for 2.5 h. Three vials of particle suspensions were then made by diluting the heated HSA solution (initial concentration 1 mg/mL) at 1:10 dilution (final concentration 0.1 mg/mL) into filtered phosphate buffer and stored in three precleaned and labeled PFA vials.

To prepare HSA aggregates by agitation, a solution of 1 mg/mL HSA was prepared as above, filtered, and split into 12 mL aliquots in three precleaned PFA vials. The HSA protein solution vials and a buffer-only vial were put on a rotator that inverted the vials once every 7.5 s to agitate the solutions for 16 to 17 h. To prepare IgG aggregates by agitation, polyclonal human IgG was obtained from Sigma Aldrich (Catalog number I2511, St. Louis, MO). Prior to use, it was diluted in sodium phosphate buffer to a final concentration of 0.30 mg/mL, filtered, and split into 11 mL aliquots in three precleaned PFA vials, and then agitated as above. The two sets of data on IgG aggregates presented in this paper were obtained from two separate lots of IgG.

In addition to the protein particle suspensions, suspensions were also produced of abraded ETFE particles. The samples and data reported in this paper for abraded ETFE particles are identical to those reported for an interlaboratory comparison on sub-visible particles (20). Briefly, the samples consisted of a polydisperse suspension of particles created from the polymer ETFE. ETFE has a low refractive index (21) (≈ 1.40 , similar to that of protein films adsorbed on surfaces (22)) and is chemically inert and mechanically strong (23). We produced polydisperse ETFE particles by first abrading ETFE against a diamond abrasive (45 μm nominal grit size, nickel bonded to a compliant backing) while submerged in an aqueous solution of 0.03 mol/L 2-[4-(2-hydroxyethyl)piperazin-1-yl]ethanesulfonic acid (HEPES) and 0.1% mass concentration sodium dodecyl sulfate (SDS), buffered to pH 6. Large particles were filtered out by passing the suspension through a nylon screen with nominal 53 μm square openings. The suspension was diluted with additional HEPES/SDS solution buffered to a pH of 7.5 to give a particle count of $\approx 11,000 \text{ mL}^{-1}$ for $d \geq 1 \mu\text{m}$, which was high enough to give particle concentrations of $\approx 100 \text{ mL}^{-1}$ for $d \geq 25 \mu\text{m}$ and low enough to avoid significant coincidence errors in light obscuration instruments. Prior to use, the HEPES/SDS solution was filtered through a 0.45 μm PVDF syringe filter (Millex-HV,

EMD Millipore, Billerica, MA, USA). The large concentration of SDS proved necessary to promote dispersion of the highly hydrophobic ETFE particles: measurements on suspensions with an SDS concentration below 0.03% mass concentration had poor repeatability. The suspension was packaged in PFA screw-top vials with flat interior bottoms that had been precleaned by agitation in 0.1% mass concentration SDS, followed by two agitations in ultrafiltered water.

For calibration of the flow imaging instruments, suspensions of silica beads were used. We verified the size by measurement on a calibrated light obscuration particle counter (PAMAS, Leonberg, Germany, model SVSS-C with a HCB-LD-25/25 sensor head). The beads of 25.0 μm nominal diameter gave anomalous results; measurements of the 10.3 and 25.0 μm beads in a calibrated microscope gave measured diameters of 10.2 and 19.9 μm , respectively. The refractive index of the silica beads was determined by immersion of the beads in either glycerol-water or 2-pyridinemethanol-water mixtures, and using quantitative phase imaging (QPI; see the section below for a discussion of QPI). The 1.57 and 6.1 μm beads had an approximate refractive index of 1.43; the 10.2 and 19.9 μm beads had a refractive index of approximately 1.47, close to that of bulk silica.

The beads were suspended in a matrix liquid of $\approx 16.5\%$ glycerol (by mass) in water for the 1.57 and 6.1 μm beads, and $\approx 50\%$ glycerol (by mass) in water for the 10.2 and 19.9 μm beads. The resulting liquid had a refractive index difference between the beads and the matrix fluid of 0.07, approximately corresponding to the refractive index of typical protein films adsorbed on surfaces (22). Prior to use, the water-glycerol solution was filtered through a 0.45 μm PVDF syringe filter (Millex-HV, EMD Millipore, Billerica, MA, USA). The refractive index of prepared mixtures was measured at the sodium D line (589 nm wavelength), using an Abbe refractometer that had been calibrated using ultrafiltered water. Then we formed suspensions in matrix solution by adding beads, shaking vigorously for 40 s, sonicating for 60 s, and then degassing for 1 h before measurements.

Characterizing the Optical Properties of Protein Particles

For an accurate model of the light scattering by a particle, one must know or measure the average refractive index of the particles of interest. Several groups have submerged protein particles in fluids of known refractive index to determine the refractive index of the particle (15,24). However, the refractive index value obtained is the refractive index of the portions of the particle inaccessible to fluid exchange, and not the desired, spatially averaged refractive index.

To obtain a better measure of the spatially averaged refractive index, the refractive index of the protein particles was determined using QPI. There are many approaches to obtain quantitative phase images (25). We have chosen to implement

a method based on the Transport of Intensity Equation, in which changes in brightfield image intensity with a shift in the focal plane can be mathematically related to the optical phase shift introduced by the test sample (26–28). Compared to other methods, one advantage of this approach is that the images can be obtained with standard microscope hardware.

The particle suspensions of interest were pipetted into a Palmer Chamber and two brightfield images were obtained for each particle at a focal plane separation of 2 μm , using Kohler illumination, 20 \times magnification, and incoherent green (530 nm) illumination. The QPI algorithm was implemented using custom software that was optimized for phase detection of particles by automatically breaking up an image into sub-images, each containing a single particle. The software also incorporated a hand-drawn mask around each particle, fixing the phase outside the mask boundaries at zero and thereby improving the accuracy of the phase determination.

The technique of quantitative phase imaging produces a phase map of the apparent optical phase difference $\phi(x, y)$, which is proportional to the difference in optical thickness between the particle and the matrix liquid:

$$\phi(x, y) = \frac{2\pi\Delta n z_p}{\lambda_0}, \quad (1)$$

where Δn is the average refractive index difference between the particle and the matrix liquid, z_p is the thickness of the particle in the vertical z direction, x and y are lateral dimensions in the image plane, and λ_0 is the wavelength of light in vacuum.

For small particles (diameter less than 10 μm), the accuracy of QPI is limited by the optical resolution of the microscope images. When the brightfield images are converted to phase maps, the mathematical algorithm introduces further blurring. As a result, the phase values smear out near the edge of each particle. For our optical set-up, profiles through the phase map for spherical beads gave an inflection point at phase values approximately 20% of the maximum phase value of the particle. This same 20% threshold corresponded reasonably well with the actual particle edge for beads. Motivated by this observation, the refractive index of the particles was inferred from the average phase of the largest 80% of $\phi(x, y)$ values. We assumed that the protein particles could be modeled as prolate spheroids. For a prolate spheroid, the relation of the refractive index to the average of $\phi(x, y)$ over a fraction F of the highest phase values is obtained by integration of Eq. 1 to obtain:

$$\langle \Delta n \rangle = \frac{3}{4\pi} \frac{\lambda_0}{\eta^{1/2} d} \frac{(1 - (1 - F)^2)}{(1 - (1 - F)^3)}, \quad (2)$$

where d is the equivalent circular diameter of the imaged particle area, and η is the aspect ratio of minor to major axis.

Equation 2, with $F=0.8$, was applied to QPI measurements of $\phi(x, y)$. Although the particles deviated significantly from spheroidal geometry, we could not identify a more accurate yet still practical solution. The values of η and d were obtained for each particle using the particle-fitting capabilities of ImageJ (29).

The quantitative accuracy of QPI is potentially limited by the arbitrariness of this choice of threshold and by the apparent dependence of the QPI results on the coherence of the light source. Published literature for objects with a thickness comparable to the width and length report that correcting phase values from the thin-object algorithm of Paganin and Nugent (27) (Eq. 1) by a factor C_d of either two (28) (using white light illumination) or one (30) (using highly coherent light). In our implementation, we used partially coherent green light. To determine the correction factor appropriate for our apparatus and algorithm, we prepared suspensions of both glass beads and PMMA beads. Glass beads were suspended in glycerol ($\Delta n=0.041$) and in a mineral oil and bromonaphthalene (BN) mixture ($\Delta n=-0.023$); PMMA beads were suspended in 2-pyridinemethanol (2P) ($\Delta n=0.0215$) and in glycerol ($\Delta n=0.0175$). Figure 1a shows the correction factor C_d to multiply the measured refractive index from Eq. 2 to obtain the correct refractive index. The results agree qualitatively with that of Bellair *et al.* (28), but we find that correction factor is smaller at large diameters (1.35 instead of 2.0) and that the increase in C_d occurs at smaller diameters than in Ref. 28.

There is a separate correction factor to Eq. 2 accounting for the deviation of the protein particles from a circular cross section. When the particles settle onto a glass side, the most gravitationally stable state is with the thinnest dimension of the particle along the vertical axis. The ratio between the height and width of the protein particles was assessed by first obtaining stacks of images using an automated objective scanner (31) (40 \times objective, 0.55 NA, positioned by a MIPOS 100 scanner from Piezo Jena GmbH, Jena, Germany) for at least 20 particles of each type. The ratio of the height to width was obtained from the ratio of the minimum Feret diameter in the x - y plane to the maximal z distance between in-focus regions of the particle seen in the obtained image stack. In this calculation, the scanned z distance was multiplied by the refractive index of the buffer to account for shifts in the focal point caused by beam refraction.

If the phase measured by QPI was independent of the thickness to width ratio t/w , then the correction factor for the refractive index would simply be w/t . However, the greater sensitivity of QPI for thin objects ($t < w$) partially offsets this correction. This effect introduces a second correction factor, $C_{w/t}$ so that the relation between measured and actual refractive index of an object is given by:

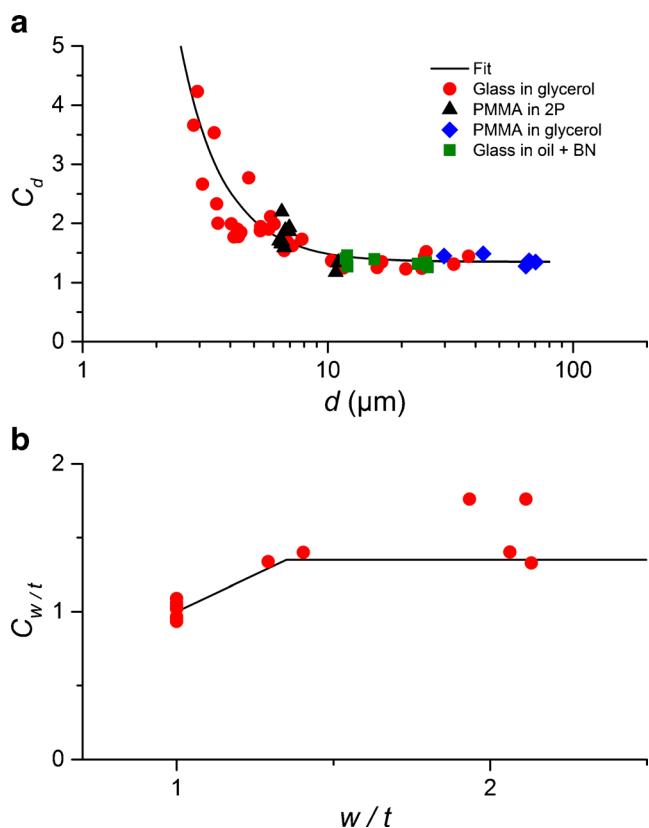


Fig. 1 Correction factors in Eq. 3: **(a)** correction factor C_d as a function of diameter for a variety of bead-liquid suspensions. The black line is a power law plus a constant that was fit to the data, **(b)** correction factor $C_{w/t}$, as a function of the ratio of particle width to thickness w/t . The black line was used to parameterize $C_{w/t}$.

$$\langle \Delta n \rangle_{\text{actual}} = \frac{w}{t} \frac{C_d}{C_{w/t}} \langle \Delta n \rangle_{\text{meas}}, \quad (3)$$

To determine $C_{w/t}$, we prepared flattened spheres of PMMA by dusting a microscope slide with nominal $69 \mu\text{m}$ PMMA spheres, adding a cover slip, heating on a hot plate to the softening point of PMMA, and then gently compressing the spheres by applying pressure to the cover slip. The gap between the slide and the cover slip was filled with glycerol, and the compressed beads measured by the QPI method. The thickness was determined by measuring the distance between the two glass surfaces (facilitated by using intentionally dirty slides and cover slips). The results for this correction factor $C_{w/t}$ are shown in Fig. 1b. The line is a parameterization of the results, subject to the constraint that the maximum value for $C_{w/t}$ cannot exceed the value of C_d .

A schematic of this work flow, along with sample images, is given in Fig. S2 in the Supplementary Information.

Particle Sizing and Counting

The prepared samples were measured by light obscuration and by flow imaging. For the light obscuration results, a light

obscuration particle counter (PAMAS Leonberg, Germany, model SVSS-C with a HCB-LD-25/25 sensor head, operating at a wavelength of $0.67 \mu\text{m}$) was used. An additional light obscuration system (Hach Co., Loveland, CO: HIAC ABS2 autosampler with a 9064 counter and a HRLD 150 sensor head, operating at a wavelength of $0.83 \mu\text{m}$) was used for measurements to characterize the differences between the PAMAS and HIAC properties. For flow imaging, two instruments were used. A Micro-Flow Imaging DPA-4200 (ProteinSimple, San Jose, CA; settings: $4 \times$ objective, $100 \mu\text{m}$ thick flow cell, at set point 3) is henceforth designated “imaging system A”. A FlowCAM bench top instrument (Fluid Imaging Technologies, Yarmouth, ME; settings: $10 \times$ objective, $100 \mu\text{m}$ thick flow cell, area-based diameter, capture thresholds of 12 dark and 8 light, 5 close hole iterations) is designated “imaging system B”. All three instruments had been calibrated for diameter with polystyrene beads, and count accuracy was confirmed by measurement of commercial PSL count standards.

Protein particle suspensions were degassed for 60 min prior to measurement, by placing in a vacuum desiccator at $\approx 200 \text{ kPa}$ atmospheric pressure (32). Because protein particles may either dissociate back to protein monomer or continue to grow, we performed the measurements on all three instruments as expeditiously as possible. The prepared samples were measured by light obscuration and by flow microscopy in triplicate in the morning, and for each round, the measurements on all three instruments were in quick succession. For particle counting measurements, triplicate measurements were performed on three separate vials of particle suspensions. Then on the afternoon of the same day, QPI measurements were performed. The agitated-HSA particles were especially susceptible to changes in particle concentration upon repeated measurement. To mitigate this effect, the vial was mixed gently and then nearly simultaneous measurements were started on all three instruments. The ETFE particles are much more stable than protein particles and the particle count and QPI measurements were taken within a 2 month span.

Methods to Model the Bias of Light Obscuration Counters

Relation of Scattering to Reported Diameter

In a light obscuration particle counter, the test solution passes through a flow cell which is traversed by a collimated laser. A particle passing through the beam will scatter and absorb light, reducing the transmitted beam intensity. The reduction in the beam intensity is converted to an equivalent diameter, based on calibration of the instrument with polystyrene latex beads of several known diameters. For protein particles and PSL beads, light absorption is negligible, and the optical cross section is the result of light scattering. The ratio between the

optical cross section of a particle and the physical projected area of a particle, A_p , is described as the extinction efficiency factor Q :

$$Q = \frac{C_{\text{sca}}}{A_p} = \frac{C_{\text{sca}}}{\pi(d/2)^2}, \quad (4)$$

where C_{sca} is the scattering cross section and d is the equivalent diameter of a circle of the same area as A_p .

Because the instrument is calibrated with PSL beads, the instrument reports the diameter of a PSL bead with the same total scattering as the tested particle. The resulting relationship between the measured equivalent diameter, d_{meas} , the actual equivalent diameter d_{act} , the extinction factor for PSL beads, Q_{PSL} , and the extinction factor for the particle, Q is:

$$Q_{\text{PSL}}(d_{\text{meas}})^2 = Q(d_{\text{trans}})^2. \quad (5)$$

If Q_{PSL} and Q can both be calculated, then Eq. 5 provides a means of obtaining the transformed equivalent diameter d_{trans} from the indicated d_{meas} (the transformed diameter is the best estimate of the actual particle diameter). First, Q_{PSL} and Q are calculated for a range of d values. Then, d_{meas} is fixed at one of the d values used for the calculation, and the corresponding d_{trans} value is found by linear interpolation of the right hand side of Eq. 5. The resulting $(d_{\text{meas}}, d_{\text{trans}})$ pairs form a look-up table that can be used along with linear interpolation to transform measured d_{meas} values into actual particle diameters.

There are two complications in calculating Q . First, a light obscuration counter will only have a reduction in transmitted light if the light is scattered outside the field of view of the detector. The minimum scattering angle for this to take place will depend on unknown details of the flow cell, position of the particle in the flow cell, and the optical arrangement. This angle also may vary with the azimuthal angle. To avoid these complications, we assumed that there is a single effective angle α equal to the minimum angle for light to be scattered out of the detector. The Aperture Measurements section below gives a relatively simple method for determining α . Once α is known, then for any model of light scattering from a particle, the extinction efficiency factor is obtained by integrating the normalized light scattering intensity over the range of scattering angle θ from α to π , where α is the half-angle of the light obscuration detector, and then integrating again over random orientations of the spheroid. Care in integration over θ is needed, because the integrand is highly oscillatory. Low-order integration approaches (such as the trapezoid rule) are needed to obtain reliable convergence.

The second complication in implementing Eq. 5 is obtaining a reliable, yet simple, model for Q . Exact results for scattering from particles large compared to the wavelength of light are known only for a few simple geometries, such as spheres, spheroids, and cylinders. However, protein particles not only have a complex structure, but the details of the

structure are not well known or easy to measure. Our initial attempts at modeling protein particles as randomly oriented, homogeneous spheroids showed good results for particles of approximately 5 μm diameters or less. For larger particles, though, the model failed, producing large overcorrections to the predicted diameter. What we present in this paper is a hybrid theory: for particles less than a cut-off diameter (to be discussed later), the particles are modeled as homogeneous spheroids. Above the cut-off diameter, the optical scattering is scaled using a simple approximation. The approximation was motivated by theoretical results for the scattering from randomly oriented, irregular arrays of spheres. The Scaling the Efficiency Factor section below presents such a model, beginning first with a discussion of relevant scattering theories, and then proceeding to the construction of a scaling model for Q . Even simpler models, assuming constant refractive index with either spheroidal or spherical geometry, are also used for comparison. The Discussion section contains a concise summary of the complete process of correcting the bias of the LO measurements.

Aperture Measurements

The magnitude of α for the light obscuration counter was determined by measuring the apparent diameter of PMMA spheres suspended in liquids of different refractive index. We performed two separate measurements. In the first measurement, large (70 μm) PMMA spheres suspended in both water and in mineral oil of known refractive index. From literature values for the refractive indices of water (33) and PMMA (34), and certificate values for the mineral oil, the value of Δn is approximately 0.157 in a matrix fluid of water, and 0.022 in a matrix fluid of mineral oil for the 670 nm operating wavelength of the LO instrument used. Measurement of the spheres in an oil matrix required sequential flushing of the LO instrument with ethanol, n-decane, and mineral oil to obtain accurate measurements. The instrument must be flushed in the reverse sequence to return the instrument to an aqueous solution and to avoid fouling of the instrument. In the second measurement, 20 μm PMMA spheres were suspended in a glycerol-water mixture of refractive index 1.418 at a wavelength of 589 nm (approximately 58% volume fraction glycerol). The ratio of the indicated diameter in water to indicated diameter in the high-refractive-index fluid can be theoretically predicted for a fixed value of α using Mie theory. (See the [Supporting Information](#).) By comparison with the experimental value for this ratio, the effective value of α can be determined. Note that the exact diameter of the PMMA beads is not needed for this determination. Results of these two measurements gave an aperture value of 0.055 rad using 70 μm spheres and 0.056 rad for 20 μm spheres. The determination using a glycerol/water mixture has the advantage that flushing the instrument out after the measurement is very

easy, although the viscosity of the suspension may be too high to use in some instruments. Alternatively, the effective aperture could have been determined by measuring the apparent diameter of PMMA beads of known diameter in an oil matrix. Figure S1 in the Supporting Information shows the results of theory and measurement for the ratio of the indicated diameter.

To assist in determining the applicability of our results to other LO instruments, the aperture was also determined for a HIAC HRLD-150 sensor head, which was the sensor head most commonly reported in a recent intercomparison (20). The aperture measurements used 20 μm PMMA spheres in a glycerol-water mixture of refractive index 1.4201 at wavelength of 569 nm and the same method as used for the PAMAS; the result obtained was an aperture value of 0.026 rad.

Scattering Theory for Spheroids

An exact Mie theory for the scattering of light from a spheroid is available (35), but implementation of the code is quite complex. For the cases of small Δn considered here, the work of Chen (36) provides a simple relation between the scattering of a spheroid and the scattering of an equivalent sphere. We combined this relation with existing code for computing the Mie scattering from a sphere (37) to obtain the scattering intensity of a spheroid at either arbitrary orientation or at random orientation. Our code was validated by comparison with calculations using a commercial implementation of the Mie algorithm for spheres (38) and literature results for spheroids (39).

The Rayleigh-Gans-Debye (RGD) theory of light scattering is both numerically simpler and computationally much faster than Mie theory, and scattering amplitudes are known for spheroids (40) and aggregates (41). RGD theory (39,40) is traditionally stated to be valid in the limits $|m - 1| \ll 1$ and $G = 2kl(m - 1) \ll 1$, where $m = n_p/n_l$ with n_p and n_l being the refractive indices of the particle and the matrix liquid, respectively, l is the largest characteristic length of the particle, and $k = 2\pi/\lambda$. For protein particles, the results of QPI measurements show that the first condition is valid for all of the particles considered in this paper. However, for larger particles, the value of G can greatly exceed one (e.g., $G \approx 10$ for $l = 20 \mu\text{m}$, $\lambda = \lambda_0/n_l = 0.51 \mu\text{m}$, and $m - 1 = 0.02$). In certain circumstances, though, RGD theory is accurate even with large values of G . The work of Zhao (40) demonstrates that for sufficiently small $|m - 1|$, RGD theory can give results accurate to 10% for values of G greater than 1.

The polarization state of the laser light in the LO instrument was not known. However, at the particle sizes considered for this work (1 μm indicated diameter and larger), the light scatters predominantly in the forward direction where the scattering intensity is largely independent of polarization. Our calculations assumed the incident light was unpolarized.

The Supplementary Information contains sample computer code for calculating the extinction efficiency factor of a prolate spheroid, for a detector with finite aperture, using RGD theory.

Scaling the Efficiency Factor

Visual inspection of the phase maps and dark-field microscopy images of large protein particles ($d > 10 \mu\text{m}$) revealed that light scattering from large particles was spatially inhomogeneous and was dominated by regions where the protein packing density was highest.

These observations suggested that a large protein particle can be imagined as an irregular array of scattering regions of high packing density. (See Sorensen (41) for a comprehensive discussion.) As a model system, consider an assembly of N spheres of diameter a at arbitrary positions. The optical differential cross section, predicted by RGD theory and averaged over all orientations (42,43), is proportional to the sum

$$S_N(\theta) = \sum_{i=1}^N \sum_{j=1}^N \text{sinc}(2r_{ij}k\sin(\theta/2)) \approx \sum_{i=1}^N \sum_{j=1}^N \text{sinc}(r_{ij}k\theta) \quad (6)$$

where the function $\text{sinc}(x) = \sin(x)/x$, r_{ij} is the distance between spheres i and j , θ is the scattering angle, and the approximation is valid for small θ . For a single sphere, $S_N(\theta) = 1$. For multiple spheres, the sinc function is positive for arguments less than π , and oscillatory for larger arguments. Suppose that the maximum extent of the assembly is the Feret diameter b . There will be constructive interference (and consequently strong scattering) for all spheres provided that $bk\theta < \pi$. Since the LO counter is only sensitive to scattering beyond the angle α , the condition for constructive interference becomes

$$\alpha < \theta < \pi/bk \quad (7)$$

For the values of λ and α appropriate for our LO counter, the maximum possible value of b consistent with this inequality is $b_{\text{max}} = 4.6 \mu\text{m}$. In other words, scattering centers combine coherently (i.e., proportional to the square of the local number of scatterers) for distance scales less than $\approx b_{\text{max}}$, and approximately incoherently (i.e., proportional to the local number of scatterers) for larger length scales.

The refractive index difference Δn is a convenient measure of the overall packing density of protein. Motivated by the predictions of RGD theory for lengths near b_{max} , we postulate that for length scales larger than a cut-off diameter d_c that is close in magnitude to b_{max} , Q scales as the total amount of protein in the particle:

$$Q(d > d_c) = \frac{\Delta n(d)}{\Delta n(d_c)} Q(d_c) \quad (8)$$

Equation 8 is equivalent to the postulate that the local structure of a large protein particle (at the scale of d_c or smaller) is the same as that of a particle with maximum size d_c , and the large particle scatters as if composed of an incoherent assembly of particles of size d_c . Although the scaling arguments presented above motivate Eq. 8, no claim is made that Eq. 8 is anything other than a physically motivated, phenomenological model. The choice of the cut-off value d_c is discussed in Refractive Index of Particles below.

Methods to Model the Bias of Flow Imaging

Although it is well known that the results of LO counters disagree with the particle concentrations obtained from FI, different FI instruments will also give concentrations that may differ by as much as a factor of two.

For flow imaging, diameters were corrected by first measuring the diameters of five sizes of silica beads suspended in a water-glycerol mixture, as described in Preparation of Particle Suspensions above. The results of the measurements are shown in Fig. 2. The diameters of the particle suspension data were corrected by applying a simple additive correction:

$$d_{trans} = d_{meas} - c(d_{meas}) \quad , \quad (9)$$

where d_{meas} is the as-obtained diameter value, d_{trans} is the transformed diameter value, and $c(d_{meas})$ is the difference between measured and actual diameters of the silica beads. For imaging system A, there was no clear pattern to the measured values of $(d_{meas} - d_{act})|_{Silica}$, and linear interpolation was used to obtain values of the correction term between the diameters of the

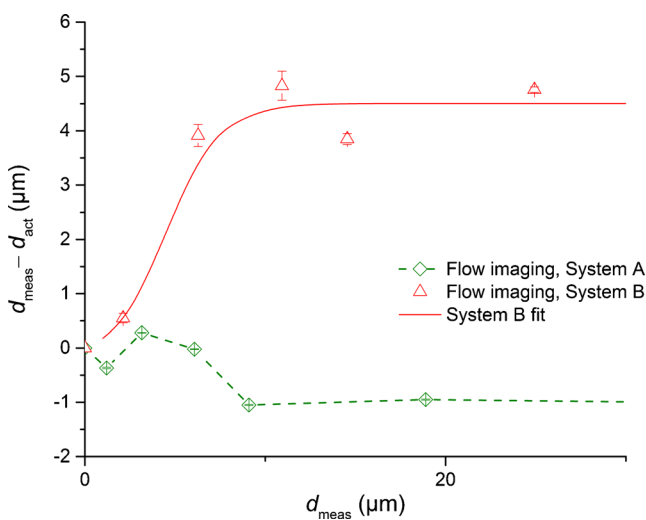


Fig. 2 The difference between the measured and actual diameters ($d_{meas} - d_{act}$) for silica beads in a water-glycerol solution versus the measured diameter, as measured by two flow imaging systems. The red line is a fit of Eq. 10 to the data for system B.

measured beads. For imaging system B, the values of $(d_{meas} - d_{act})|_{Silica}$ were fit to an equation of the form:

$$c(d_{meas}) = a_1 \tanh((d_{meas} - a_2)/a_3) + a_4 \quad , \quad (10)$$

where a_1 , a_2 , a_3 , and a_4 are parameters determined by a nonlinear least-squares fit of the equation to the measured data. The form of Eq. 10 is purely empirical and was chosen based on the observation that $c(d_{meas})$ rose smoothly to a near constant value as d_{meas} increased. Note that the particle detection thresholds for imaging system B were set to maximize the sensitivity to low-contrast particles. These settings may have given an increased offset of the correction curve.

The diameter of the smallest measured bead was $1.57 \mu\text{m}$, which is slightly larger than the minimum reported diameter of $1 \mu\text{m}$. We extended the range of the correction term to lower diameter values by assuming that at zero diameter, the correction was also zero.

RESULTS

Theoretical Results

Prior experimental (15,17) and theoretical (18) work has demonstrated that a small refractive index difference Δn , relative to that of PSL beads in water, is largely responsible for smaller indicated diameters of particles measured by light obscuration. What is not known is the importance of deviations from spherical geometry, and, for elongated particles, the importance of particle orientation relative to the optical axis. As a first effort in exploring the relative importance of these factors, we have calculated the extinction efficiency factor of prolate spheroids as a function of particle refractive index, aspect ratio, and orientation, using both Mie and RGD scattering theory. For all of the calculations, the aperture angle was set a typical value of 0.05 rad, and the vacuum wavelength was 670 nm. The particles were averaged over all orientations unless noted. Calculation of the true extinction efficiency factor requires dividing the total scattering by the projected area, which depends on both aspect ratio and particle orientation. To emphasize the variations in extinction efficiency factor that arise from variations in the scattering alone, results are reported for a modified extinction efficiency factor Q' , equal to the total scattering beyond the aperture angle, divided by the average projected area of a randomly oriented spheroid. The diameter is given as the equivalent spherical diameter.

As seen in Fig. 3, a variation of a factor of two in aspect ratio has significantly less impact on Q' than a factor of two variation in Δn , for Δn less than approximately 0.05 and aspect ratios in the range 0.25 to 1. Figure 4 demonstrates that particle orientation (either random orientation or aligned with

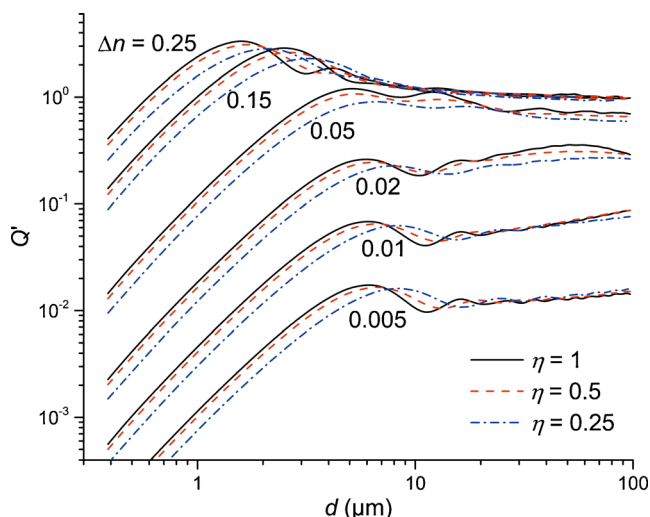


Fig. 3 Extinction efficiency factor versus effective particle diameter for prolate spheroids of varying aspect ratio and refractive index difference from a water matrix liquid. Curves represent Mie theory results for an aperture angle of 0.05 rad, vacuum wavelength of 670 nm, random particle orientation, and refractive index difference as indicated in the figure.

the flow field) has an effect comparable to variations in aspect ratio and is again a smaller effect than a two-fold variation in refractive index. Taken together, Figs. 3 and 4 illustrate that the particle refractive index is the dominant parameter affecting the strength of optical scattering.

Computations of scattering intensity for randomly oriented spheroids are numerically intensive because of the complexity of the Mie formulas and the need to integrate over the scattering angle and particle orientation. RGD theory is much more compact to program and the code executes faster. Figure 5 compares the results for Q for prolate spheroids of

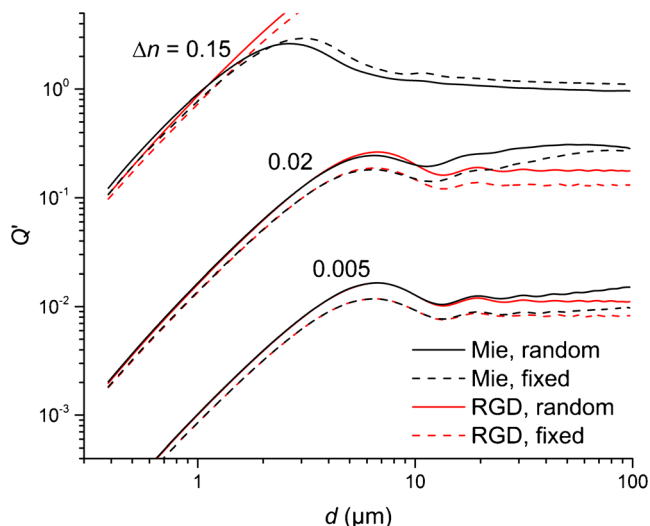


Fig. 4 Extinction efficiency factor versus effective particle diameter for prolate spheroids of either random orientation or with a major axis normal to the axis of the incident light. Theoretical curves are calculated for aspect ratio of 0.5, aperture angle of 0.05 rad, vacuum wavelength of 670 nm, and a refractive index difference as indicated in the figure, using both Mie and RGD theory.

aspect ratio 0.5 for both Mie and RGD theories. The results demonstrate that RGD theory gives values of Q that are in agreement with Mie theory to within a factor of two for $\Delta n \leq 0.05$ and effective diameter $\leq 30 \mu\text{m}$, and within 10% of Q for $\Delta n \leq 0.02$ and $d \leq 8 \mu\text{m}$. For the value $\Delta n = 0.25$ (appropriate for PSL beads in water), RGD theory is in poor agreement with Mie theory in the size range of interest here.

These results suggest that reasonable predictions of scattering can be obtained by using Mie theory for the scattering from PSL beads and RGD theory for particles of low Δn . What is surprising is the behavior of the RGD predictions of Q for particles of large diameter. In Fig. 5, for Δn of 0.05 or less, the RGD values of Q approach a constant, asymptotic value as d increases, rather than increasing to unphysically large values as seen at larger values of Δn . This behavior is a consequence of the finite detector angle of LO instruments. The scattering of particles of diameter much larger than the wavelength of light is concentrated in a narrow cone at small scattering angles (i.e., forward scattering). If this full cone of scattered light is integrated, the predicted value of Q diverges for large d values using RGD theory. However, LO instruments are only sensitive to scattering at angles greater than α , and the exclusion of smaller angles eliminates the portion of the scattered light where RGD theory fails most dramatically. (See [Supporting Information](#) for details.) For $d > 10 \mu\text{m}$, the light scattered out of the beam is largely confined to a narrow ring with a scattering angle slightly larger than α . Evaluation of the expression for Q by RGD theory in this limit gives a result independent of d , as observed in the numerical results.

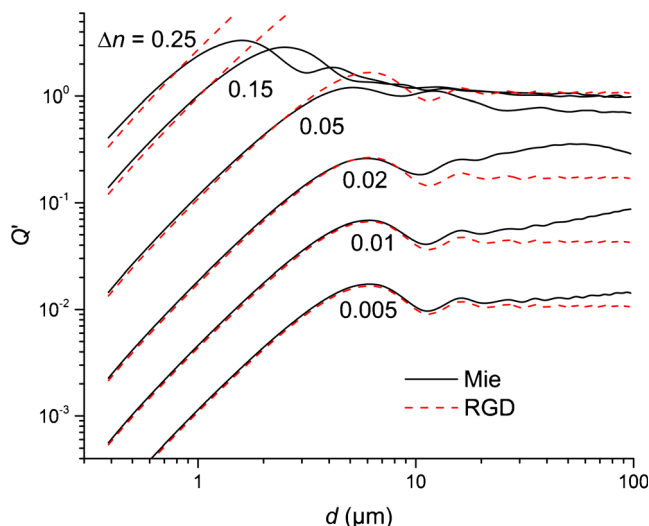


Fig. 5 Extinction efficiency factor versus effective particle diameter for prolate spheroids, as calculated by both Mie and RGD theory. Theoretical curves are calculated for an aspect ratio of 0.5, aperture angle of 0.05 rad, vacuum wavelength of 670 nm, random particle orientation, and a refractive index difference as indicated in the figure.

Refractive Index of Particles

Figure 6 shows the results of QPI measurements on typical particles from all four types of particle suspensions. Qualitatively, all four types of particle suspensions behaved the same. There is a smooth drop in Δn as the diameter increases, which was parameterized as a power law plus a constant. Comparing the values for ETFE to those of the protein particles shows that the ETFE particles and actual protein particles have similar optical contrast. There are significant differences in the Δn values measured for the two lots of agitated IgG, even though the procedures for particle creation and measurement of Δn for these two lots were nominally identical. The final transformation of diameter worked well for both of these data sets, but the variability in Δn could be an issue for applicability of this method (see Discussion).

After the refractive index values were obtained, we could study the choice of the cut-off diameter d_c . The calculated value of Q was insensitive to the choice of d_c . Detailed analysis of the Q versus diameter curves corresponding to the measured refractive index values revealed that a d_c value that would maximize the value of Q at all diameters varied from 3.9 to 5.8 μm for the different particle types. The calculated values of the scaled Q using these d_c values differed by no more than 4% for the scaled Q values calculated at $d_c = b_{\text{max}} = 4.6 \mu\text{m}$. Consequently, $d_c = 4.6 \mu\text{m}$ was used for all calculations of the scaled Q .

The scatter in the refractive index values is quite large (RSD of $\approx 50\%$), as a result of many possible factors: approximating irregular particles as a spheroid, the variable aspect ratios of the particles, and the variability of the QPI measurements (e.g., see Fig. 1a). Because the relationship between the indicated LO diameter of particle i is not a linear function of the refractive index of the particle, Δn_i , the diameter of a particle of average refractive index may not be equivalent to the average of the diameters of a set of particles of known Δn_i . To test whether the dispersion in refractive index was significant, we numerically simulated the effect on indicated diameter of replacing particles with an average Δn with a Gaussian distribution of Δn_i values. The results of the simulation showed that the observed scatter in Δn caused on average a 6% variation in indicated diameter. This error is small enough to be neglected.

There is a second effect that results from the dispersion of diameter values. Consider the case where a set of particles of identical diameter is measured, and the measuring instrument reports a range of diameter values. The effect of this variability in diameter variability may be estimated by convoluting a distribution function for the diameter variability (e.g., a Gaussian distribution) with the observed particle size distribution. Numerical simulations for the effect of diameter variability resulting from refractive index differences show approximate shifts in $N(d)$ of 6% to 25% for light obscuration. We

have not applied a correction for this effect because there are sources of indicated-diameter variability that apply to flow imaging as well (e.g., particle orientation in the flow cell, variation in image properties with position relative to the focal plane, and incorrect image boundaries for large, translucent particles). Evaluation of these factors is beyond the scope of the present paper.

Results of Scaling

As shown in the theoretical results above, the value of Q becomes sensitive to particle refractive index for $\Delta n \approx 0.05$ and below. Measurements of polydisperse silicone oil droplets illustrate the differences in particle count for different instruments for spherical particles for $\Delta n = 0.067$ (at the operating wavelength of 670 nm of the LO instrument). Figure 7a shows the results of measurements of a silicone oil suspension for a light obscuration instrument and two flow imaging instruments. Prior to scaling of the LO results and application of calibration results for the flow imaging instruments, the particle counts differ by a factor of 2 to 4 over the range 1 to 25 μm . The as-measured data were compiled as tabular values of $N(d)$ versus d . These data were rescaled by adjusting the d value for each value of $N(d)$, and replotting. Figure 7b shows the results after transformation of diameters. The transformation of the LO data used Mie theory for spheres, since the RGD theory is not reliable for $\Delta n = 0.067$ at large diameters. The transformed data agree to within a relative standard deviation (RSD) of 16%, demonstrating that calibration of the diameter response of the particle counting instruments can significantly improve the agreement between instruments.

These results are in semi-quantitative agreement with the results of Vandesteeg and Kilbert (11), which were obtained with a HIAC LO instrument. The Vandesteeg data show a reduction in LO particle concentrations relative to flow imaging of a factor of 3 at 2 μm , a peak in LO sensitivity at 5 μm , and approximate equivalence of LO and flow imaging concentration at 10 and 20 μm . In comparison, the present data shows a reduction in LO sensitivity of a factor of 2.4 at 2 μm , a peak in LO sensitivity near 8 μm , and a drop in LO sensitivity at 20 μm . The ratio of LO concentration to flow imaging concentration agrees to within 30% at 2, 5 and 10 μm . At 20 μm , the discrepancy increases to $\approx 60\%$, but because the particle size distribution is dropping so rapidly with increasing diameter, this count discrepancy is equivalent to a diameter error of only 15%. Although the exact HIAC sensor head used for the Vandesteeg work is not known, the closer agreement at diameters $> 20 \mu\text{m}$ is consistent with the smaller aperture value that we measured for the HIAC sensor head compared to the PAMAS sensor.

In contrast to the silicone oil case, correction of the LO bias for irregular particles of varying refractive index, the calculations require determination of the refractive index and aspect

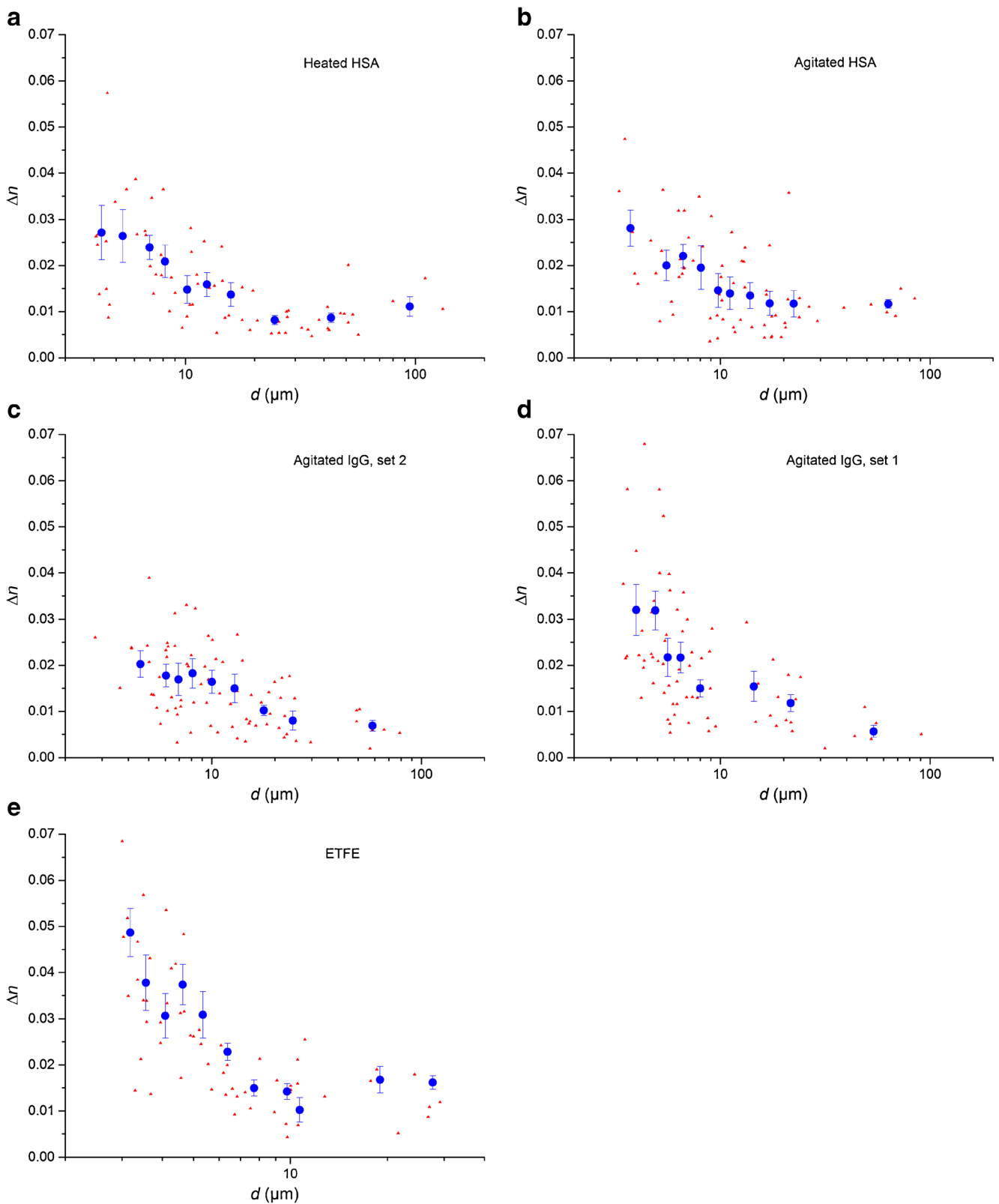
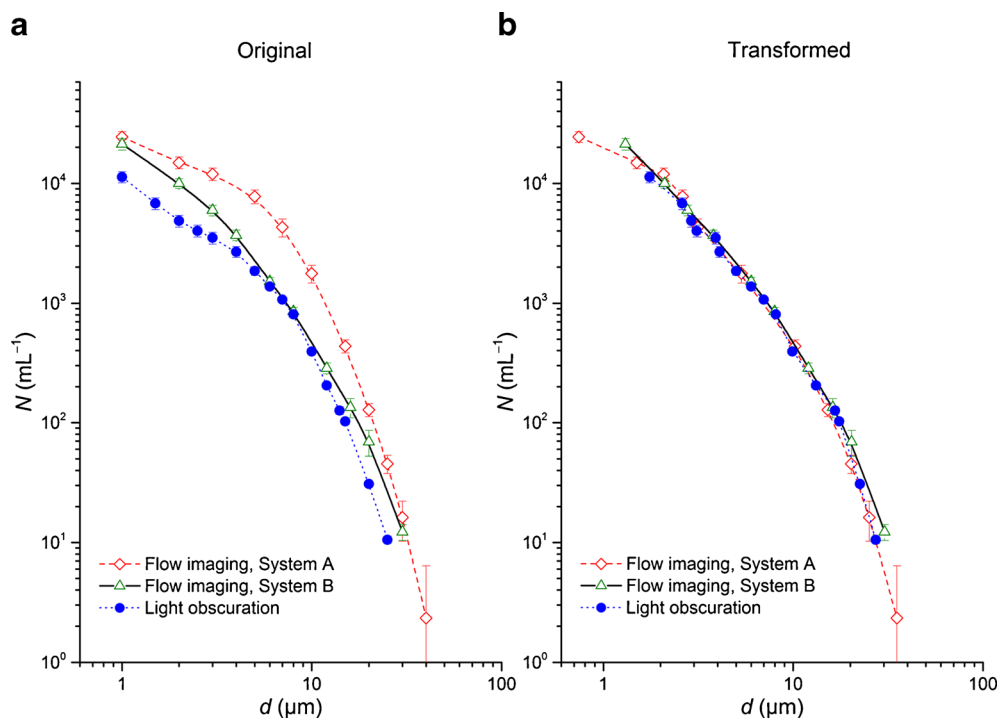


Fig. 6 Apparent refractive index of particle populations as a function of diameter. *Small red dots* indicate results for individual particles; *large blue dots* indicate average diameter and refractive index of binned data. *Error bars* indicate the standard error of the mean (SEM).

ratios of the particles, followed by generation of a scaled model of the extinction efficiency factor, Q_e .

Experimentally, particle size distributions were obtained using LO and the two flow imaging instruments for the three

Fig. 7 Original and transformed particle counts for heated HSA particles, as a function of diameter. Original data is shown in (a); transformed data in (b) have diameters adjusted for each data set. Error bars indicate SEM of the counts of three different sample vials.



protein particle suspensions and the ETFE particle suspensions. For the HSA and IgG particle suspensions, triplicate measurements were obtained for each of three independent vials. Because of concerns that the first set of vials of agitated IgG were measured with imaging system B slightly out of optimal focus, we prepared and measured a full second set of agitated IgG samples. The results for the ETFE particle suspension are those performed by NIST for a recent interlaboratory comparison (20).

The left-hand panes of Figs. 8, 9, 10, 11 and 12 show the as-obtained data for the particle size distributions $\mathcal{N}(d)$ for the four particle suspensions. The data show a consistent pattern: the values of $\mathcal{N}(d)$ for LO measurements are consistently below those of FI measurements by as much as a factor of ≈ 20 , and in the size range $\approx 2 \mu\text{m}$ to $\approx 20 \mu\text{m}$, the $\mathcal{N}(d)$ values for imaging system B exceed those of imaging system A by up to a factor of ≈ 2 .

The particle data was rescaled in the same manner as the silicone oil droplet data, but using the scaled- Q model for the LO data. After making the diameter corrections based on silica bead measurements, counts for the two flow imaging instruments agree very well throughout the range of overlap, as shown by the red and green curves in the right-hand panes of Figs. 8, 9, 10, 11 and 12.

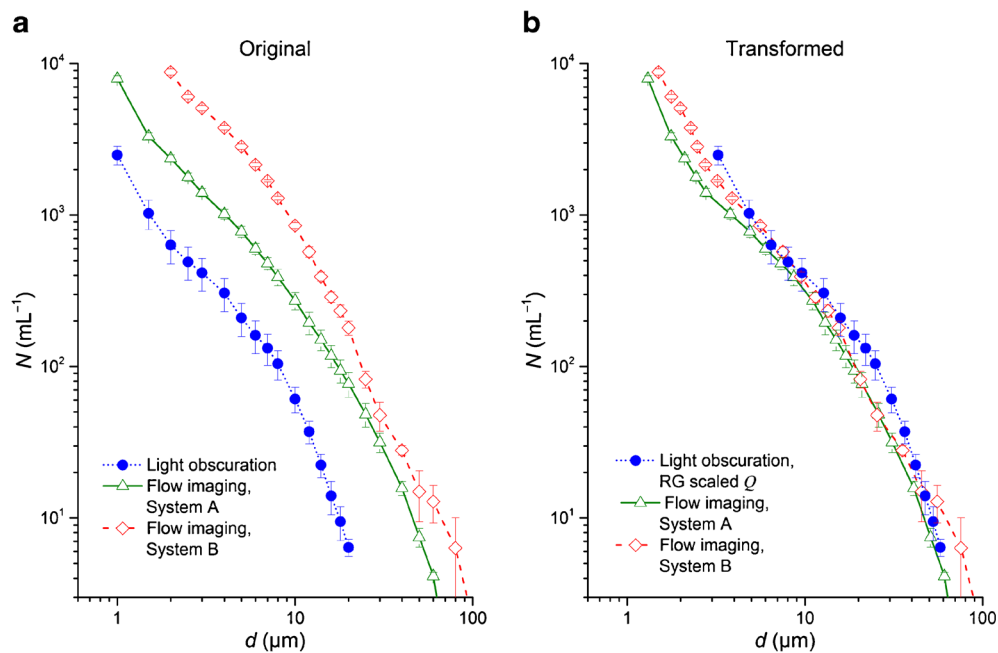
For the transformation of the LO diameters, the light scattering from the test particles was modeled using RGD theory up to a diameter of $4.6 \mu\text{m}$ and the scaling relation of Eq. 8 for larger diameters. Because the RGD theory is highly accurate for diameters less than or equal to $4.6 \mu\text{m}$, and the scaling

relation is used at higher diameters, the values of Q calculated using Mie theory differ by only 2% from the values from RGD theory. In all cases, the value of Q for PSL beads (see Eq. 5) was calculated by Mie theory, since RGD theory fails for the large Δn values of PSL beads in aqueous buffer. For each vial, the average aspect ratio was obtained by averaging all aspect ratio values from the three runs on flow imaging system B. Figures 8, 9, 10, 11 and 12 present the results of the original and transformed data using RGD-theory plus scaling model.

The agreement of the transformed data is excellent for all particle types, except for diameters $> 40 \mu\text{m}$ for ETFE, $> 60 \mu\text{m}$ for agitated IgG, and in the region near $20 \mu\text{m}$ for agitated HSA. The level of agreement between the data sets can be readily quantified. Table I gives a summary of the level of agreement of the data before and after transformation, expressed as the ratio $R_{\mathcal{N}(d)}$ of the maximum value of $\mathcal{N}(d)$ for the three instruments divided by the minimum value of $\mathcal{N}(d)$. Prior to the diameter transformations, $R_{\mathcal{N}}$ for the three instruments and for the five types of droplet and particle suspensions ranged from 3.1 to 48 over the size range from 2 to $20 \mu\text{m}$, with an average ratio of 14.5. After correction of instrument biases, the disagreement was substantially reduced in the region of overlap (5 to $25 \mu\text{m}$) for all of the optical models used to transform the LO data, as shown in Table I. In the region of overlapping LO and FI data (5 to $25 \mu\text{m}$), the average value of $R_{\mathcal{N}}$ is reduced to an average value in the range from 1.3 to 1.7 (See Table II).

Because of the labor involved in fully characterizing Δn as a function of diameter, we explored an alternate model with Δn

Fig. 8 Original and transformed particle counts for heated HSA particles, as a function of diameter. Original data is shown in (a); transformed data in (b) have diameters adjusted for each data set. Error bars indicate SEM of the counts of three different sample vials.



set as a constant, taking Δn as the value at $d = 4.6 \mu\text{m}$, and using either Mie or RGD theory over the full range of d . Results of the transformation for agitated HSA are shown in Fig. S2 in the Supplementary Information as an example. The transformed results for the Mie theory show a significant discrepancy in N with the LO values less than the FI values for $d > 30 \mu\text{m}$. Interestingly, the RGD theory of this model with constant Δn gives LO values that agree very well with FI results. Figure 4 shows that at Δn near 0.02, the RGD

approximation underestimates Q , and this underestimation likely compensates for values of Δn that are too large at $d > 30 \mu\text{m}$.

DISCUSSION

The overall success of the diameter transformation illustrates that LO and FI data sets that disagree by more than a factor of

Fig. 9 Original and transformed particle counts for agitated HSA particles, as a function of diameter. Original data is shown in (a); transformed data in (b) have diameters adjusted for each data set. Error bars indicate SEM of the counts of three different sample vials.

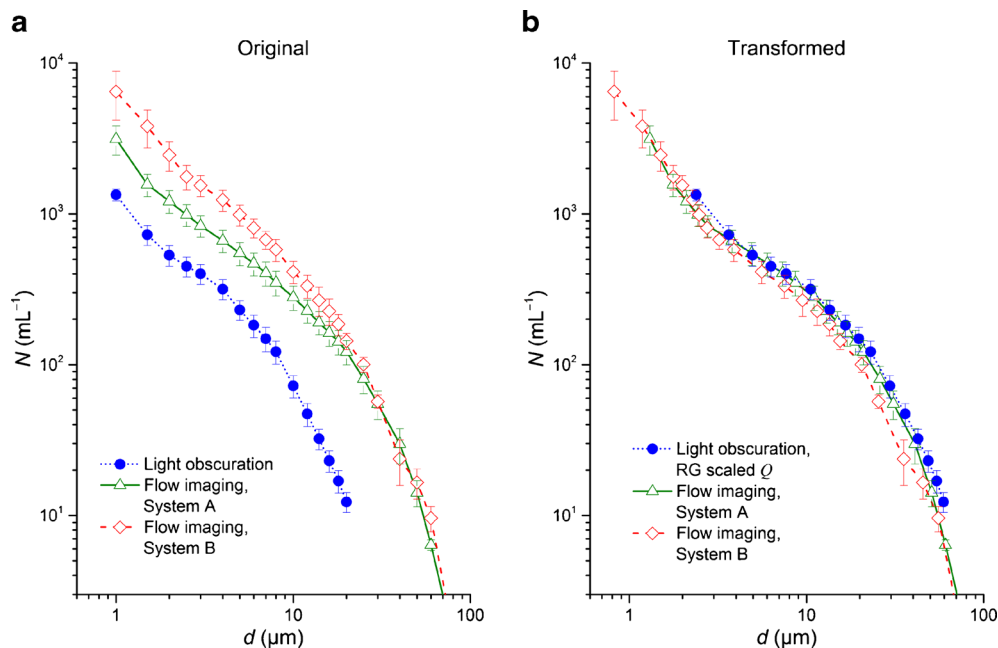
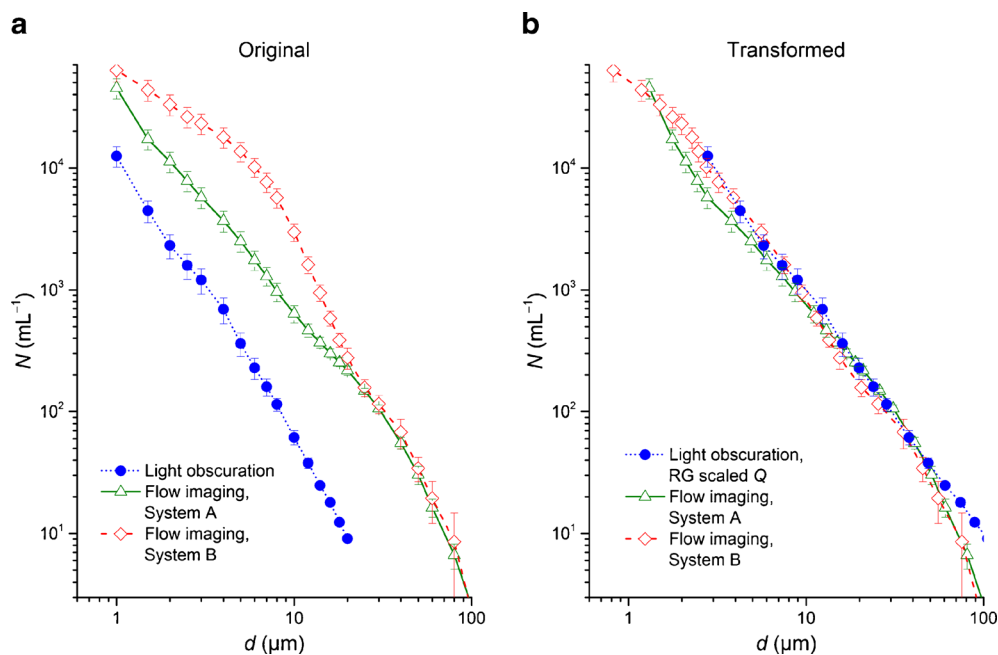


Fig. 10 Original and transformed particle counts for agitated IgG particles (run 1), as a function of diameter. Original data is shown in (a); transformed data in (b) have diameters adjusted for each data set. Error bars indicate SEM of the counts of three different sample vials.



ten in concentration can be reconciled in a quantitative manner by transforming indicated diameters in accordance with simple calibration schemes or instrument models. A number of issues make modeling of the LO instrument response appear initially intractable:

1. The geometry of LO instruments is generally proprietary and not available to customers.
2. Protein particle morphology is variable and not well characterized.
3. The range of size and the refractive index difference between the particle and the matrix fluid, Δn , on initial analysis appear to be outside the range where simple optical approximations work well.
4. The distribution of protein within a particle is likely inhomogeneous, and the scattering from an inhomogeneous

Fig. 11 Original and transformed particle counts for agitated IgG particles (run 2), as a function of diameter. Original data is shown in (a); transformed data in (b) have diameters adjusted for each data set. Error bars indicate SEM of the counts of three different sample vials.

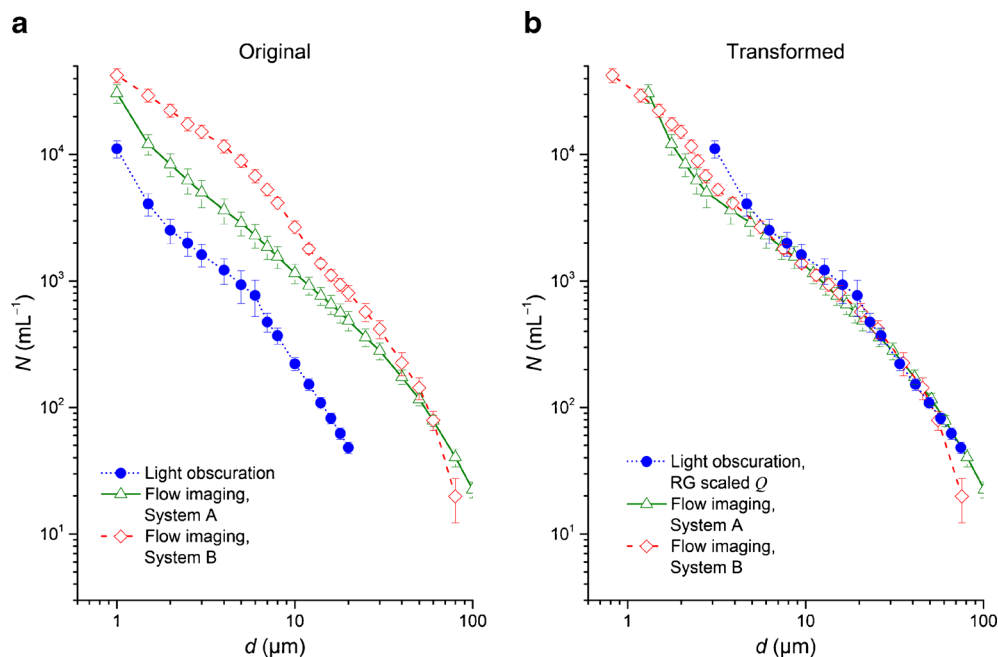
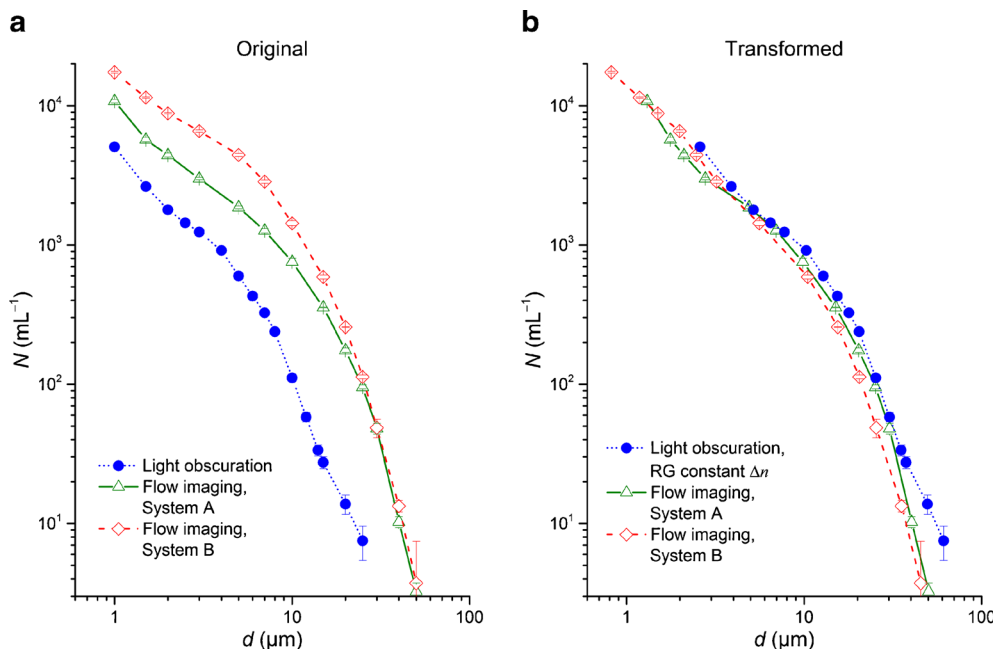


Fig. 12 Original and transformed particle counts for abraded ETFE particles, as a function of diameter. Original data is shown in (a); transformed data in (b) have diameters adjusted for each data set. Error bars indicate SEM of the counts of three different sample vials.



particle can be much higher than a homogeneous particle.

Table I Level of Agreement Between Three Data Sets (One Light Obscuration And Two Flow Imaging), Before and After Bias Correction, for Different Particle Types. The Table Gives the Ratio $R_N = N_{max}/N_{min}$, where N_{max} and N_{min} are the Maximum and Minimum Values of $N(d)$ for the Five Data Sets, at a Fixed Value of d

	Diameter d					
	1 μm	2 μm	5 μm	10 μm	20 μm	25 μm
Silicone oil						
As measured	2.17	3.07	4.19	4.49	4.14	4.31
RGD scaled Q	NA	1.25 ^a	1.17	1.51	1.61	1.86
Heated HSA						
As measured	4.86	4.61	4.29	5.72	11.70	NA
RGD scaled Q	NA	1.18 ^a	1.18	1.29	1.42	1.72
Agitated HSA						
As measured	9.47	13.91	13.53	13.97	28.16	NA
RGD scaled Q	NA	1.93 ^a	1.29	1.20	1.76	2.06
Agitated IgG, Set 1						
As measured	5.05	14.36	37.73	48.0	30.42	NA
RGD scaled Q	NA	1.81 ^a	1.50	1.29	1.42	1.34
Agitated IgG, Set 2						
As measured	3.81	8.86	9.54	12.07	16.76	NA
RGD scaled Q	NA	1.62 ^a	1.28	1.18	1.38	1.13
Abraded ETFE						
As measured	3.43	4.94	7.40	12.93	18.59	15.04
RGD scaled Q	NA	1.38 ^a	1.14	1.50	2.06	2.24

^a Flow imaging data only

The approach presented in this paper largely overcomes the above issues:

1. The only geometric attribute needed for the LO instrument is the effective detector aperture.
2. The response model is based on known formulas for the scattering of light by a spheroid. By comparing nearly exact calculations based on Mie theory (37) to simple approximations using the RGD theory (42), we demonstrate that because of the particular geometry of LO instruments, the simple RGD theory is much more accurate than initial estimates would suggest.
3. To incorporate particle inhomogeneity, we use properties of the RGD theory to motivate a simple scaling method. The scaling method also reduces the maximum diameter for which the RGD theory needs to be applied.
4. Measurement of the effective refractive index of the particles by quantitative phase imaging, together with the application of the scaling method, sufficiently characterizes the protein morphology.

For flow imaging instruments, the use of silica beads to generate a five-point calibration curve proved to be highly

Table II Maximum, Minimum, and Average Values of the Ratio $R_N = N_{max}/N_{min}$, Before and After Bias Correction, Averaged Over the Four Particle and One Droplet Types for the Indicated Diameter Ranges

	Maximum	Minimum	Average
As measured ($d = 2 \mu\text{m}$ to $20 \mu\text{m}$)	48.0	3.07	14.5
Transformed ($d = 5 \mu\text{m}$ to $25 \mu\text{m}$)			
RGD scaled Q	2.24	1.13	1.47

effective in reducing the relative bias between instruments of different makes and optical configuration. However, there may remain an absolute bias of the imaging instruments for several reasons. At the smallest diameters where all three data sets overlap, the LO values for N are consistently higher than the flow imaging values. While not as prone to bias as LO instruments, the diameters indicated by FI instruments are influenced by the particle refractive index, especially for particle sizes of a few micrometers (15,17,44). The silica-bead calibration scheme may not accurately account for this effect, or may require tuning of the optimal Δn between silica beads and the matrix liquid. At large diameters, a silica-bead based correction scheme does not account for possible miscounting of extended particles that are detected as multiple smaller particles, nor does it accurately model size errors due to diffraction effects for elongated particles (45). With these limitations in mind, the present results demonstrate that two FI instruments with significantly different designs can give particle size distributions in close agreement when calibrated in the same manner. These additional factors will increase in importance with higher protein or excipient concentration. We hope to address these issues in a future publication.

For light obscuration instruments, the diameter corrections are somewhat more complex, requiring a one-time determination of the instrument aperture, a measurement of the typical refractive index of the particles being measured, and a calculation of the extinction efficiency factor Q . For the refractive index measurements, the QPI algorithm as discussed in the Methods section is not presently commercially available. A different QPI method has been implemented in a commercial instruments and may provide a more convenient method of generating particle phase maps (46). The calculations do not require extensive software or computational power, though. RGD theory closely agreed with the Mie theory results for light scattering from protein particles, which allows use of computational codes that are simpler and faster than the complex codes to describe scattering of randomly oriented spheroids by Mie scattering. The success of the model for Q implies that the LO instrument response depends primarily on only two parameters: the refractive index of the particles and the effective aperture of the LO instrument, with a weak dependence on particle aspect ratio.

The theoretical results (Fig. 3) for Q show that values of Q for $d > 4 \mu\text{m}$ vary little between $\Delta n = 0.05$ and $\Delta n = 0.25$. As a result, LO instruments significantly undersize particles only if Δn is less than ≈ 0.05 , or if the particle morphology is sufficiently irregular that modeling the particle as a spheroid of fixed refractive index is a poor approximation. Literature values of Δn obtained by immersion of aggregates in liquids of varying refractive index give Δn values of 0.09 to 0.13 (15,25). Modeling of particles as homogeneous spheroids with these refractive indices cannot explain the large degree of undersizing by LO seen in our data, which necessitated our direct

measurements of particle refractive index by QPI. A method of estimating particle mass based on particle morphology may also allow use of a smaller set of QPI results (47).

There are three significant limitations of the method presented in this paper. First and most fundamentally, the method only works if the particle counts are dominated by a single particle type. If there is a mixture of particle types (e.g., silicone oil droplets and protein particles), light obscuration cannot distinguish between these types. Modeling of the light scattering of a heterogeneous population can only be done if the relative particle size distributions are known for each particle type, and such an effort would be very difficult.

Second, the theory assumes that the particles are randomly oriented. In fact, we have observed that plate-like particles tend to align in the plane of the flow cell, and rod-like particles tend to align along the flow axis (45). The calculations shown in Fig. 5 demonstrate that this effect could have a significant effect.

A more practical issue is that the QPI measurements to determine the refractive index of the particles are laborious. The QPI measurements for particles of diameter less than $3 \mu\text{m}$ are likely not accurate because of the limited optical resolution at this size scale. Measurements of the refractive index of particles generated by a variety of stresses and for a variety of therapeutic protein types, protein concentrations, and excipient concentrations would be useful to establish how the refractive index difference Δn between the particles and the matrix fluid depends on the stress, formulation, and protein type. The differences observed for Δn for the two lots of IgG raise the concern that Δn values may not be reproducible from lot to lot. The variability of Δn values should be studied for different proteins and protein formulations.

The procedure for correcting the bias of light obscuration measurements has multiple steps, as given in detail in the Methods section of the main paper. These steps are outlined below to provide the reader with a concise summary of the complete procedure.

Procedure:

1. Experimentally determine the effective aperture α of the light obscuration instrument (this needs to be done only once)
2. Determine the accuracy and any needed correction terms for the QPI measurement using beads in several liquids (this needs to be done only once)
3. Using Mie theory and the value of α , calculate the extinction efficiency factor for PSL beads *versus* diameter, $Q_{\text{psl}}(d)$ (this needs to be done only once)
4. For a given particle suspension type, acquire a stack of microscopic images that fully brackets the particle depth for a number of particles.
5. From two images near the center of the stack, obtain the phase map of a selection of particles.

6. Correct the refractive index, using Eq. 3.
7. Convert the phase map to refractive index *versus* particle diameter, using Eq. 2, and obtain the effective diameter from the phase map or the brightfield images.
8. For particle diameters less than the cut-off diameter d_c , model the particles as homogeneous spheroids of refractive index $n(d)$, and use RGD theory to predict the extinction efficiency factor Q .
9. For particle diameters greater than d_c , obtain Q by scaling $Q(d_c)$ according to Eq. 7.
10. Obtain a diameter scale correction using Eq. 4.

Of these steps, steps 1 and 2 are not difficult and need be done only once, and steps 7–9 are straightforward. Step 3 requires careful work but only needs to be done once. The difficult and laborious task is to adequately characterize the spatially averaged refractive index of the particles. Although the methods presented in this paper were fully successful, they are not practical for routine laboratory use. As mentioned above, commercial implementations of steps 4 and 5 may improve the practicality of determining the refractive index. Alternatively, approximate corrections may be possible if the refractive index differences of protein particles are correlated by applied stress, protein type, and protein concentration.

A separate issue for the broad applicability of these corrections is whether the diameter corrections found here apply to similar instruments in other laboratories. An international comparison of abraded ETFE particles (20) provides a large data set of LO and FI values of $\mathcal{N}(d)$. The comparison data revealed that there was no significant difference in response between the two primary manufacturers of LO instruments, provided that the sensor heads were designed for maximum particle sizes of 200 μm or below. There was a statistically significant difference between the results of two manufacturers of FI systems, as we see in this paper as well. From the compiled comparison data, we created three data: LO data with restricted sensor heads, FI data for the same instrument manufacturer as System A, and FI data for the same manufacturer as System B and restricted to $10\times$ magnification. These three data sets can be analyzed exactly as we have analyzed our data in the Results section. The diameter transformation is remarkably effective at removing biases between the data sets. By applying the diameter transformation found in the present paper to the three data sets, the discrepancy drops from an average value of $R_N=12.6$ for the original data to a value of only 1.18 for the transformed data, in the 5 to 20 μm range where the data overlap. The excellent agreement provides evidence that the diameter transformations for the ETFE particles are generally uniform for similar instruments. As further evidence of the applicability of these results, the LO diameter transformation was compared for both a HIAC HRLD-150 sensor ($\alpha=0.026$ rad and $\lambda_0=0.83$ μm) and a PAMAS HCB-LD-25/25 sensor ($\alpha=0.026$ rad and $\lambda_0=0.83$ μm). Over a

particle size range from 2 to 60 μm , the ratio of PAMAS transformed diameter differed from the HIAC transformed diameter by no more than 23%, and the average of the ratio of PAMAS to HIAC diameters was 1.04. This result corroborates the agreement of the HIAC and PAMAS data sets in the ETFE comparison.

CONCLUSION

In this work, we demonstrate that it is possible to correct the relative biases and get good quantitative agreement for particle concentration in the range 2 to 25 μm , for two different flow imaging instruments and a light obscuration instrument.

Significantly, success depended on accurately characterizing the spatially averaged refractive index of the measured particles, but did not depend on knowing the detailed morphology of the particles. This conclusion has important ramifications for the development of reference materials for standardizing particle counting instruments. The success of the bias correction procedures in the present paper was in large part due to the careful characterization of the refractive index of the protein particles. Developing simple methods to tune the difference in refractive index between the reference-material particles and the matrix fluid, and match this particle suspension to a test-sample suspension, will likely be necessary. The greatest challenge for broad implementation of the method is the lack of a rapid method for determining the spatially averaged refractive index of particles relative to the fluid matrix, as a function of diameter.

The scattering theory used for the LO transformation of the protein and ETFE particles is derived from methods shown to work for highly irregular aggregated material and should be applicable to irregular protein aggregates or other spatially non-uniform but chemically well defined aggregates. The theory will likely not work well for chemically heterogeneous aggregates (e.g., air bubbles or silicone oil associated with protein aggregates) for which the scattering is much stronger than for pure protein aggregates. The theory also does not fully account for the scattering of very elongated particles (lengths greater than ≈ 30 μm) (45). Although the theory is appropriate for particles of low Δn that are likely to be present in solutions with high monomer or excipient concentrations, the effects of high opalescence that often occur in such solutions are not included in the model.

The procedure for correcting the bias of flow imaging instruments has fewer steps and is easier to implement than the bias correction of light obscuration instruments. Future work, however, needs to be done to understand how to correct the biases in FI instruments in cases of high protein or excipient concentration and to incorporate a correction for deviations of non-spherical particle morphology (45).

This work may also have utility in designing LO instruments that have reduced sensitivity to particle refractive index and in modeling the sensitivity of LO instruments to mixtures of different particle types with different refractive indices, such as silicone oil and aggregated protein particles.

ACKNOWLEDGMENTS AND DISCLOSURES

We thank Wyatt Vreeland of the National Institute of Standards and Technology for helpful comments, Robert Fletcher of the National Institute of Standards and Technology for assistance with aperture measurements, and Nathan Vandesteeg of Baxter Healthcare for further details of his work.

REFERENCES

- Carpenter JF, Randolph TW, Jiskoot W, Crommelin DJ, Middaugh CR, Winter G, *et al.* Overlooking subvisible particles in therapeutic protein products: gaps that may compromise product quality. *J Pharm Sci.* 2009;98(4):1201–5.
- Rosenberg AS. Effects of protein aggregates: an immunologic perspective. *AAPS J.* 2006;8(3):E501–507.
- Rosenberg AS, Verthelyi D, Cherney BW. Managing uncertainty: a perspective on risk pertaining to product quality attributes as they bear on immunogenicity of therapeutic proteins. *J Pharm Sci.* 2012;101(10):3560–7.
- Filipe V, Jiskoot W, Basmelch AH, Halim A, Schellekens H, Brinks V. Immunogenicity of different stressed IgG monoclonal antibody formulations in immune tolerant transgenic mice. *mAbs.* 2012;4(6):740–52.
- Bi V, Jawa V, Joubert MK, Kaliyaperumal A, Eakin C, Richmond K, *et al.* Development of a human antibody tolerant mouse model to assess the immunogenicity risk due to aggregated biotherapeutics. *J Pharm Sci.* 2013;102(10):3545–55.
- USP/NF Monograph <787>. Subvisible particulate matter in therapeutic protein injections. In. Rockville, MD: United States Pharmacopeial Convention; 2014.
- USP/NF Monograph <788>. Particulate matter in injections. In. Rockville, MD: United States Pharmacopeial Convention; 2014.
- Sharma DK, King D, Oma P, Merchant C. Micro-flow imaging: flow microscopy applied to sub-visible particulate analysis in protein formulations. *AAPS J.* 2010;12(3):455–64.
- Zolls S, Tantipolphan R, Wiggenhorn M, Winter G, Jiskoot W, Friess W, *et al.* Particles in therapeutic protein formulations, part 1: overview of analytical methods. *J Pharm Sci.* 2012;101(3):914–35.
- Strehl R, Rombach-Riegraf V, Diez M, Egodage K, Bluemel M, Jeschke M, *et al.* Discrimination between silicone oil droplets and protein aggregates in biopharmaceuticals: a novel multiparametric image filter for sub-visible particles in microflow imaging analysis. *Pharm Res.* 2012;29(2):594–602.
- Vandesteeg N, Kilbert C. Differentiation of subvisible silicone oil droplets from irregular standard dust particles. *J Pharm Sci.* 2013;102(6):1696–700.
- Sharma DK, Oma P, Pollo MJ, Sukumar M. Quantification and characterization of subvisible proteinaceous particles in opalescent mAb formulations using micro-flow imaging. *J Pharm Sci.* 2010;99(6):2628–42.
- Singh SK, Afonina N, Awwad M, Bechtold-Peters K, Blue JT, Chou D, *et al.* An industry perspective on the monitoring of subvisible particles as a quality attribute for protein therapeutics. *J Pharm Sci.* 2010;99(8):3302–21.
- Huang CT, Sharma D, Oma P, Krishnamurthy R. Quantitation of protein particles in parenteral solutions using micro-flow imaging. *J Pharm Sci.* 2009;98(9):3058–71.
- Zolls S, Gregoritz M, Tantipolphan R, Wiggenhorn M, Winter G, Friess W, *et al.* How subvisible particles become invisible-relevance of the refractive index for protein particle analysis. *J Pharm Sci.* 2013;102(5):1434–46.
- Barnard JG, Rhyner MN, Carpenter JF. Critical evaluation and guidance for using the Coulter method for counting subvisible particles in protein solutions. *J Pharm Sci.* 2012;101(1):140–53.
- Werk T, Volkin DB, Mahler HC. Effect of solution properties on the counting and sizing of subvisible particle standards as measured by light obscuration and digital imaging methods. *Eur J Pharm Sci.* 2014;53:95–108.
- Knollenberg RG, Gallant RC. Refractive index effects on particle size measurements in liquid media by optical extinction. In. International Conference on Particle Detection; 1990. p. 154–182.
- Ripple DC, Dimitrova MN. Protein particles: what we know and what we do not know. *J Pharm Sci.* 2012;101(10):3568–79.
- Ripple DC, Montgomery CB, Hu Z. An interlaboratory comparison of sizing and counting of subvisible particles mimicking protein aggregates. *J Pharm Sci.* 2015;104:666–77.
- French RH, Rodriguez-Parada JM, Yang MK, Derryberry RA, Lemon MF, Brown MJ, Haeger CR, Samuels SL, Romano EC, Richardson RE. Optical properties of materials for concentrator photovoltaic systems. *Ieee Phot Spec Conf.* 2009:149–154.
- Voros J. The density and refractive index of adsorbing protein layers. *Biophys J.* 2004;87(1):553–61.
- DuPont(tm) Tefzel(R) fluoropolymer resin, properties handbook. 2015 February 10. Available from: http://www2.dupont.com/KIV/zh_CN/assets/downloads/h96518.pdf.
- Totoki S, Yamamoto G, Tsumoto K, Uchiyama S, Fukui K. Quantitative laser diffraction method for the assessment of protein subvisible particles. *J Pharm Sci.* 2015;104(2):618–26.
- Mir M, Bhaduri B, Wang R, Zhu RY, Popescu G. Quantitative phase imaging. *Prog Opt.* 2012;57:133–217.
- Teague MR. Deterministic phase retrieval - a green-function solution. *J Opt Soc Am.* 1983;73(11):1434–41.
- Paganin D, Nugent KA. Noninterferometric phase imaging with partially coherent light. *Phys Rev Lett.* 1998;80(12):2586–9.
- Bellair CJ, Curl CL, Allman BE, Harris PJ, Roberts A, Delbridge LM, *et al.* Quantitative phase amplitude microscopy IV: imaging thick specimens. *J Microsc.* 2004;214(Pt 1):62–9.
- Rasband WS. ImageJ, U. S. National Institutes of Health, Bethesda, Maryland, USA. 2015 February 10. Available from: <http://imagej.nih.gov/ij/>.
- Frank J, Matrisch J, Horstmann J, Altmeyer S, Wernicke G. Refractive index determination of transparent samples by noniterative phase retrieval. *Appl Opt.* 2011;50(4):427–33.
- Edelstein AD, Tsuchida MA, Amodaj N, Pinkard H, Vale RD, Stuurman N. Advanced methods of microscope control using µManager software. *J Biol Methods.* 2014;1(2), e11.
- Cao S, Jiang Y, Narhi L. A light-obscuration method for quantifying subvisible particles in protein therapeutics. *Pharm Forum.* 2010;36(3):824–34.
- Daimon M, Masumura A. Measurement of the refractive index of distilled water from the near-infrared region to the ultraviolet region. *Appl Opt.* 2007;46(18):3811–20.
- Kasarova SN, Sultanova NG, Ivanov CD, Nikolov ID. Analysis of the dispersion of optical plastic materials. *Opt Mater.* 2007;29(11):1481–90.

35. Asano S, Yamamoto G. Light scattering by a spheroidal particle. *Appl Opt.* 1975;14(1):29–49.
36. Chen TW. Effective sphere for spheroid in light-scattering. *Opt Commun.* 1995;114(3–4):199–202.
37. Bohren CF, Huffman DR. Absorption and scattering of light by small particles: Wiley Science; 1998.
38. MiePlot, vers. 4.3.05. 2015 February 10. Available from: <http://www.philiplaven.com/mieplot.htm>.
39. Barber PW, Wang DS. Rayleigh-Gans-Debye applicability to scattering by nonspherical particles. *Appl Opt.* 1978;17(5):797–803.
40. Zhao Y, Ma L. Applicable range of the Rayleigh-Debye-Gans theory for calculating the scattering matrix of soot aggregates. *Appl Opt.* 2009;48(3):591–7.
41. Sorensen CM. Light scattering by fractal aggregates: a review. *Aerosol Sci Technol.* 2001;35(2):648–87.
42. Van de Hulst HC. Light scattering by small particles. New York: Wiley; 1957.
43. Olaofe GO. Scattering by 2 Rayleigh-Debye Spheres. *Appl Opt.* 1970;9(2):429–38.
44. Hu Z, Ripple DC. The use of index-matched beads in optical particle counters. *J Res Natl Inst Stand Technol.* 2014;119:674–82.
45. Cavicchi RE, Carrier MJ, Cohen JB, Boger S, Montgomery CB, Hu Z, *et al.* Particle shape effects on subvisible particle sizing measurements. *J Pharm Sci.* 2015;104(3):971–87.
46. Bon P, Maucort G, Wattellier B, Monneret S. Quadriwave lateral shearing interferometry for quantitative phase microscopy of living cells. *Opt Express.* 2009;17:13080–94.
47. Kalonia C, Kumru OS, Prajapati I, Mathaes R, Engert J, Zhou S, *et al.* Calculating the mass of subvisible protein particles with improved accuracy using microflow imaging data. *J Pharm Sci.* 2015;104(2):536–47.